Computation of Tone Noises Generated in Viscous Flows

Ching Y. Loh
Taitech Inc.
Cleveland, Ohio 44135
Email: Ching.Y.Loh@grc.nasa.gov

Philip C.E. Jorgenson
National Aeronautics and Space Administration
Glenn Research Center at Lewis Field
Cleveland, Ohio 44135
Email: Jorgenson@nasa.gov

Abstract

Three benchmark problems from the current and previous CAA workshops involving tone noise generated in viscous flows are investigated using the CE/SE finite volume method. The CE/SE method is first briefly reviewed. Then, the benchmark problems, namely, flow past a single cylinder (CAA Workshop II problem), flow past twin cylinders (from the current CAA Workshop IV, Category 5, Problem 1) and flow past a deep cavity with overhang (CAA Workshop III problem) are investigated. Generally good results are obtained in comparison with the experimental data.

1 Introduction

The space-time conservation element and solution element (CE/SE) method [1,2] is a recently developed numerical method for solving conservation laws. Despite its formal second order accuracy in both space and time, it possesses low dispersion errors and low dissipation. The method may be categorized as a finite volume method, where the conservation element (CE) is equivalent to a finite control volume (cell) and the solution element (SE) can be understood as the space-time cell interface. The CE/SE scheme features:

1. conservation in both space and time—integral form of the governing equations is solved;
2. accurate (space-time) surface flux calculation;
3. conservative variables and their gradients are considered as unknowns—leads to improved accuracy using a compact cell stencil;
4. simple but effective non-reflecting boundary conditions (NRBC);
5. MILES (monotonically integrated large eddy simulation) type scheme [12, 13], the finite volume cell average process works as a spatial filter and the weighted average (van Albada) limiter plays a role somewhat like a subgrid scale (SGS) model;
6. naturally adapted to unstructured grids, relatively effortless implementation of computation—no numerical fix or parameter choice is needed;
7. robust enough to cover a wide spectrum of compressible flow—from weak linear acoustic waves to shocks—and appropriate for both CFD and CAA.

In this paper, the two-dimensional unstructured Navier-Stokes/Euler CE/SE solver is briefly described in §2. Based on this scheme, numerical investigations of the benchmark problems are presented consequently in §3, §4 and §5, with comparisons to experimental data.

2 The Two-Dimensional CE/SE Navier-Stokes/Euler Scheme

2.1 *Conservation form of the unsteady Euler equations*

Consider a dimensionless conservation form of the unsteady Euler equations for a perfect gas. Let ρ, u, v, p, and γ be the density, streamwise velocity component, transverse velocity component, static pressure, and constant specific heat ratio, respectively. The two-dimensional Euler equations then can be written in the following vector form:

$$\mathbf{U}_t + \mathbf{F}_x + \mathbf{G}_y = \mathbf{0}, \tag{1}$$

where x, y, and t are the streamwise, transverse, and time coordinates, respectively. The conservative flow variable vector $\mathbf{U}$ is given by

$$\mathbf{U} = \begin{pmatrix} U_1 \\ U_2 \\ U_3 \\ U_4 \end{pmatrix} = \begin{pmatrix} \rho \\ \rho u \\ \rho v \\ \rho e \end{pmatrix}, \quad e = p/\rho(\gamma - 1) + (u^2 + v^2)/2, \tag{2}$$

and the flux vectors $\mathbf{F}$ and $\mathbf{G}$ (including viscous fluxes) can be written in terms of $\mathbf{U}$. By considering (x, y, t) as coordinates of a three-dimensional Euclidean space E_3 and using the Gauss divergence theorem, it follows that Eq. (1) is equivalent to the following integral equation:

$$\oint_{S(V)} \mathbf{H}_m \cdot \mathrm{d}\mathbf{S} = \mathbf{0}, \qquad m = 1, 2, 3, 4, \tag{3}$$

where $S(V)$ is the surface around a volume V in E_3 and $\mathbf{H}_m = (F_m, G_m, U_m)$, $m = 1, 2, 3, 4$.

2.2 *Conservative updating*

In any explicit time-marching scheme, flow data at neighboring nodes at the previous time step are used to update flow data at the current node to the present time level. In most finite volume schemes a computational cell (e.g., the triangular cylinder with base ΔABC in Fig. 1, left plot) is used as a control volume (CV). The first step is to determine the fluxes on its surfaces (e.g., $ABB'A'$ in Fig. 1, left plot). In the CE/SE algorithm, where not only the conservative flow variables, $\mathbf{U}$, but also their spatial derivatives are considered as unknowns (12 scalar unknowns in total), the CV is extended to a hexagon cylinder, with all the neighboring cell centers (D, E, F) included as vertices (Fig. 1, left plot). All of the surfaces (SEs) of the new composite CV, except the top surface (hexagon), are now associated with one of the three neighboring cell centers (D, E, F), where $\mathbf{U}$, $\mathbf{U_x}$, and $\mathbf{U_y}$ are known (at time step n). The advantage is that no extrapolation through the CV interior is needed in determining the fluxes. Furthermore, in order to achieve high resolution, flow data are computed by Taylor expansion from D to the centroids of the quadrilateral surfaces $ADD'A'$, $DBB'D'$ and $ADBO$, etc., *along* their surface planes. Compared to other updating techniques, conservative updating is truly multi-dimensional. It avoids the uncertainty of dimensional-splitting and extrapolation, and hence yields better accuracy.

2.3 *Evaluation of spatial gradients*

Applying Eq. (3) to the composite CV in Fig. 1 (left plot) directly yields $\mathbf{U^{n+1}}$ at the centroid of the top hexagon. Note that this location, in general, does not coincide with the triangle center O'. Furthermore, there are three hexagon cylinder composite CVs that partially overlap the current one. Because of this, three sets of derivatives, $\mathbf{U_x^{(i)}}$, $\mathbf{U_y^{(i)}}$, $i = 1, 2, 3$, can be constructed. The final values of the spatial derivatives at the current centroid, as well as at O', are obtained by applying the extended van Albada limiter (weighted average) to these, i.e.,

$$\mathbf{U_x^{n+1}} = \frac{\mathbf{\Sigma U_x^{(i)} \phi_i}}{\mathbf{\Sigma \phi_i}}, \quad \mathbf{U_y^{n+1}} = \frac{\mathbf{\Sigma U_y^{(i)} \phi_i}}{\mathbf{\Sigma \phi_i}},$$

where $\phi_i = \tau_i^{-1}$ if $\tau_i \neq 0$ and $\phi_i = 0$ otherwise; and $\tau_i = [(\mathbf{U_x^{(i)}})^2 + (\mathbf{U_y^{(i)}})^2]^\alpha$, with α being any positive real index number. Finally, having determined $\mathbf{U_x^{n+1}}$ and $\mathbf{U_y^{n+1}}$, the solution $\mathbf{U^{n+1}}$ may now be transferred to the triangle center O'.

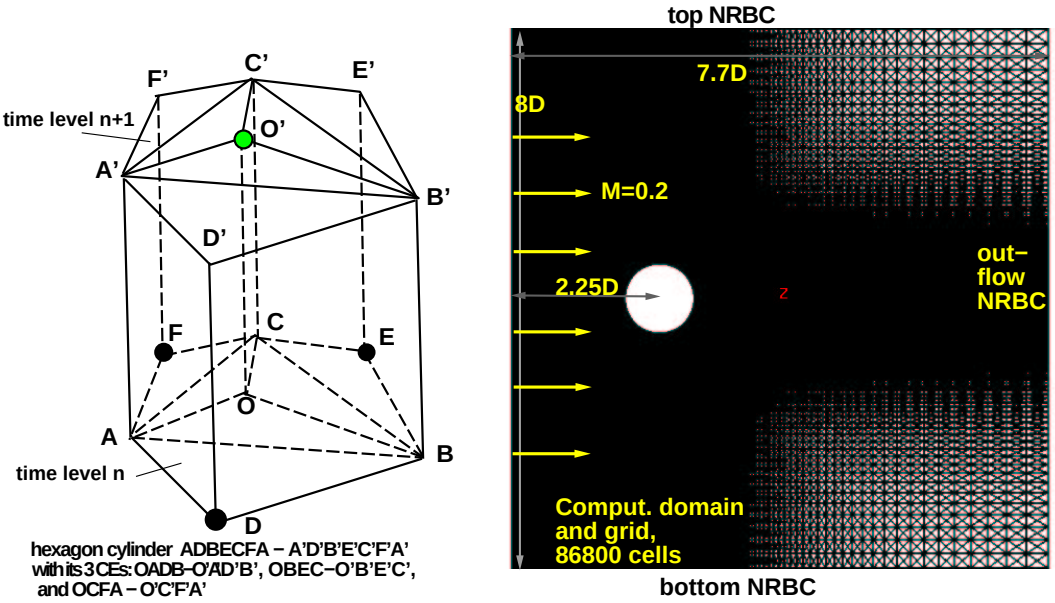

Figure 1. Left plot: CE/SE unstructured grid; three CEs and the hexagon cylinder CV in E_3; Right plot: Geometry of the computational domain and unstructured grid, $-2.2D \leqslant x \leqslant 5.5D$, $-4D \leqslant y \leqslant 4D$ for the one cylinder aeolian noise problem; seven exponentially stretched rectangular cells (as sponge zones) at the top and bottom are not shown.

2.4 *Non-reflecting boundary conditions (NRBCs)*

In the CE/SE scheme, NRBCs are constructed based on the first principle of plane wave propagation [3 , 5]. There are various variants of the NRBCs [5-8], the following are the NRBCs employed in the present paper. For a grid node (j, n) lying at the outer border of the domain, where j is the grid node index number and n the time step, the Type I NRBC requires that

$$(\mathbf{U_x})_{\mathbf{j}}^{\mathbf{n}} = (\mathbf{U_y})_{\mathbf{j}}^{\mathbf{n}} = \mathbf{0},$$

while $\mathbf{U}_{\mathbf{j}}^{\mathbf{n}}$ is kept fixed at the initially given steady boundary value. At the outflow boundary, where there are substantial gradients in the radial direction, the Type II NRBC requires that

$$(\mathbf{U_x})_{\mathbf{j}}^{\mathbf{n}} = \mathbf{0}, \quad \mathbf{U}_{\mathbf{j}}^{\mathbf{n}} = \mathbf{U}_{\mathbf{j'}}^{\mathbf{n}} \quad (\mathbf{U_y})_{\mathbf{j}}^{\mathbf{n}} = (\mathbf{U_y})_{\mathbf{j'}}^{\mathbf{n}}.$$

where j' is the nearest interior node. As will be observed later, generally, these NRBCs are robust enough to allow a near field computation without disturbing or distorting the flow and acoustic fields.

3 Aeolian Noise from a Single Cylinder (CAA Workshop II)

The current section and the two consequent sections are devoted to the numerical solution of the three benchmark problems. In this section, numerical results for the aeolian noise of a single cylinder [4] are presented and compared to their respective experimental data [9].

Consider a Mach number, M, of 0.2 uniform flow past a two-dimensional circular cylinder with a diameter, D, of $1.9cm$. Many researchers employ large computational domains comparable to the wavelength of the tone noises. In the present work, a relatively small near field computational domain is chosen. The domain size is only a fraction of the wave-length of the tone noise. The Fourier data sampling point is placed at a location beyond the reach of hydrodynamic waves (or vortex street) such that only aeroacoustic data is obtained.

Figure 1 (right plot) shows a sketch of the computational domain and the triangulated grid. The grid is obtained by dividing a rectangular cell into 4 triangles. By so doing, the advantage is that the cell size, which is important in aeroacoustics computation, is well-controlled. The diameter of the circular cylinder, the ambient speed of sound, and the ambient flow density are chosen as the scales for length, velocity, and density respectively. Although the grid

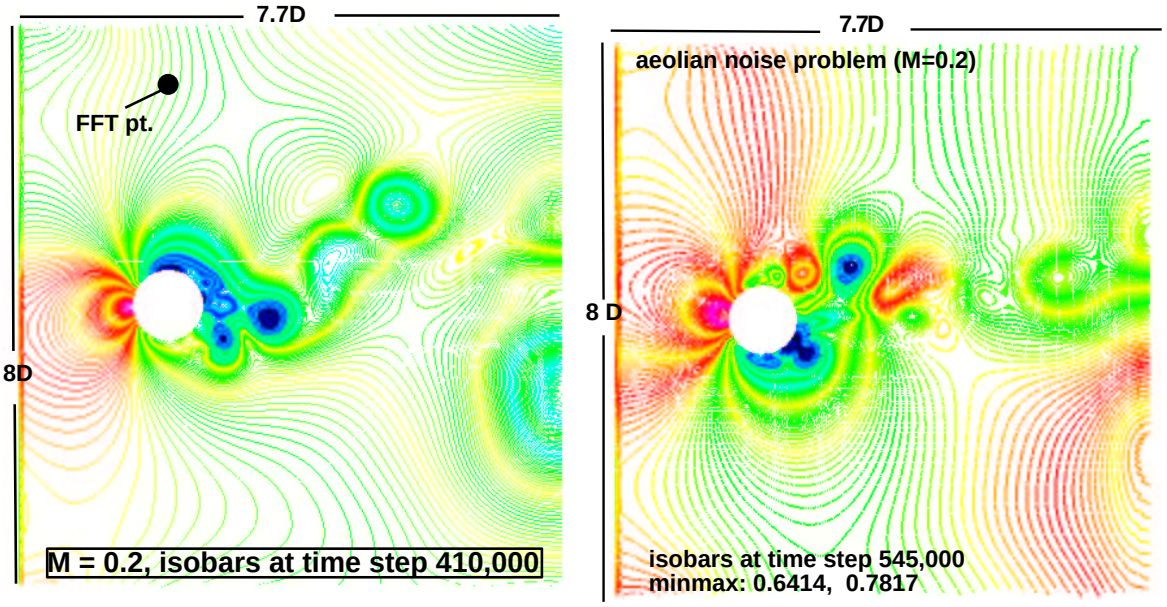

Figure 2. Instantaneous isobars.

size is the smallest at the cylinder wall, it is not fine enough to resolve the details in the boundary layers. Still, good aeroacoustic data is collected. Even if the boundary layer is well resolved with a much refined grid (at a higher CPU cost), the boundary layer details will still be lost after flow separation and vortex roll-up, so they contribute very little to large scale turbulence and aeroacoustics.

3.1 *Initial conditions*

The entire flow field is initialized at ambient conditions, *i.e.*,

$$\rho_0 = 1.0, \quad u_0 = 0, \quad v_0 = 0, \quad p_0 = 1/\gamma,$$

All spatial derivatives are set to zero.

3.2 *Boundary conditions*

At the inflow boundary, the flow variables are specified as a uniform flow with a Mach number of 0.2:

$$\rho_i = 1.0, \quad u_i = 0.2, \quad v_i = 0, \quad p_i = 1/\gamma,$$

and their spatial derivatives are set to zero. Note that these inlet conditions also play a role as absorbing boundary conditions in the CE/SE scheme(Type I NRBC). At the surface of the circular cylinder, the no-slip wall condition is applied. The upper and lower boundaries are specified as Type I NRBCs. A Type II NRBC is applied at the outflow boundary.

3.3 *The unsteady flow and the vortex street*

In order to have a reasonable time series sampling size for FFT (fast Fourier transform) analysis, with a non-dimensional time step size of 0.005, over a half million time steps are run. Figure 2 shows the isobars at time step 410,000 and 545,000. The unsteadiness and the Karman vortex street in the wake are clearly illustrated. A point located at $(0D, 3.25D)$ is selected for recording the time series. At this location, there is no direct influence from the Karman vortex street. Figure 3 (left plot) depicts the result of the FFT, i.e., the sound pressure level (SPL) vs. frequency at this selected location. The SPL in dB is relative to the level of 20 μPa.

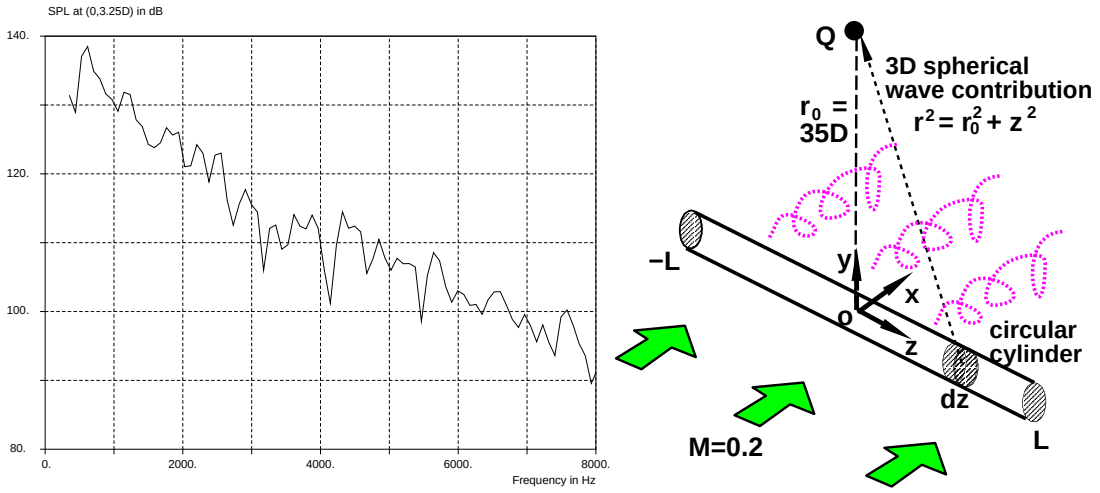

Figure 3. Left plot: Sound pressure level for Re=90,000 at (0, 3.25D), the highest peak corresponds to 617 Hz and 138 dB; Right plot: Estimate SPL at 35D, 90^o.

3.4 *Tone noise frequency*

At a Reynolds number, Re, of 90,000 the highest peak of SPL in the plot corresponds to a computed frequency of 617 Hz (with a 3dB 'bandwidth' or binwidth of 88 Hz), which is quite close to the experimental one of 643 Hz [9] at this flow condition. A numerical experiment with a "very high" Reynolds number is also tested. The computed frequency is 652 Hz, which is slightly higher but still within a 4% range of the experimental value of 643 Hz. The phenomenon that the frequency (or Strouhal number) does not significantly change near this range of Re is justified by experimental observation (see Schlichting [10]) and also agrees with the observation of Townsend [11] that the large scale turbulence only weakly depends on the Reynolds number. The term "very high" used here is a synonym of turning off the viscous terms in the scheme. As a result of the numerical damping in the scheme, viscous effects still exist.

3.5 *Sound pressure level of the tone noise*

There is no direct comparison of the sound pressure level (SPL) to the experimental data which is of a three-dimensional nature and measured at a location $35D$ away from the circular cylinder center [9]. However, after some approximation and simple analysis from first principles, an estimated SPL for three-dimensional flow SPL at $r_0 = 35D$ at a point 90^o to the flow direction can be obtained, Fig. 3, (right plot).

From the two-dimensional computation, at the point $(0D, 3.25D)$ (see the 'FFT point' in Fig. 2, left plot), an SPL of 138 dB is obtained. If the noise source is regarded to be a simple one and is located approximately at the circular cylinder centerline, for 2-D flow, the SPL attenuation is inversely proportional to r^2, where r is the distance from the source to the measuring point. Therefore, at the point Q $(0, 35D)$ the SPL is estimated to be:

$$SPL_{2d} = 138 - 20log(35D/3.25D) = 117.9dB.$$

This result is obtained under the two-dimensional assumption that the circular cylinder is infinitely long.

According to the experiment [9], a cylinder of length $10D$ is used. The point Q is assumed to be at the mid-plane normal to the cylinder centerline (the z direction), the cylinder rod ranges from $z = -5D$ to $z = 5D$. For a truly three-dimensional flow, let $p(z)$ be the r.m.s. pressure contribution from a line segment dz at z (coordinates along the cylinder centerline) to Q. Then

$$p(z) = \frac{r_0^2}{r_0^2 + z^2} p_0, \quad p_0 = p(0).$$

Table 1. **SPL of aeolian tone noise at 90^o angle**

r (distance)	Experiment [9]	CE/SE numerical
3.25D		138 dB
35D	111 dB	110.4 dB (estimated)

Generally, let L be the half length of the cylinder, the square of the total sound pressure at Q is

$$p_L{}^2 = \int_{-L}^{L} p_0^2 \frac{dz}{[1+(z/r_0)^2]^2} = r_0 p_0^2[\alpha_0 + 0.5sin(2\alpha_0)],$$

where $\alpha_0 = tan^{-1}(L/r_0)$. Let $L = 5D$ and $L = \infty$ respectively and the ratio

$$R = \frac{p_{5D}^2}{p_\infty^2} = 0.1794612$$

Therefore, the sound pressure level at Q is estimated as:

$$SPL_{3d} = SPL_{2d} + 10logR = 110.4dB$$

Table 1 compares the numerical SPLs at these two locations at an angle of 90^o with the available experimental data. Recall that the basic computation is two-dimensional, while the experimental data is for a circular cylinder of finite length in three-dimensional space. The agreement in this case is excellent.

4 Aeolian noise from twin cylinders (CAA Workshop IV)

Consider a uniform flow with a Mach number of 0.0714 (corresponding to the free stream velocity $24.5m/s$) past a pair of side-by-side two-dimensional circular cylinders with diameters, D, of $0.955cm$ and located $3D$ apart (center to center). A large computational domain is chosen in order to study the development of the vortex streets in the wake. The domain ranges $-12D \leqslant x \leqslant 30D$ and $-12D \leqslant y \leqslant 12D$ and has about 684000 unstructured triangular cells. The origin $(0,0)$ corresponds to the mid-point between the two cylinder centers. Instead of using a triangulated structured grid as in the previous problem, a truly unstructured triangular grid generated by Gridgen is used. Figure 4 (left plot) illustrates the grid around one of the cylinders. The purpose here is to find out how well a truly unstructured grid performs. The domain is decomposed into 8-12 subdomains using METIS and MPI is used to run the code on a parallel PC cluster.

After the Workshop, the same problem is run using another grid with smaller domain size $-3D \leqslant x \leqslant 5.5D$, $-6.5D \leqslant y \leqslant 6.5D$ and about 130,000 triangular cells are employed. Though the domain is much smaller, triangular cells are refined and relatively uniform around the wake area of the twin cylinders, rendering better aeroacoustic resolution.

The diameter of the circular cylinders, the ambient speed of sound ($a_0 = 343m/s$), and the ambient flow density are chosen as the scales for length, velocity, and density respectively. The initial and boundary conditions are almost identical to the previous problem except the free stream Mach number is smaller ($M = 0.0714$).

4.1 *Development of the vortex streets in the wakes*

Figures 4-6 illustrate respectively the snapshots of isobars, Mach number, and vorticity contours at time step 1.1 million. Near the twin cylinders, the contours exhibit symmetry with respect to the horizontal center line. This implies that the noise source is of the 'dipole' type. Around $20D$ downstream of the twin cylinders, the flow becomes highly asymmetrical, and vortex pairing occurs. However, since turbulence should have been fully developed in reality at this location, it is not clear that they represent true physics or just numerical artifacts due to the two-dimensional computation.

It should also be noted that at the workshop presentation, we presented the time-averaged p'^2, which is the true time averaged p'^2 which include the hydrodynamic waves in the vortex streets. It should *not* be interpreted or compared to the acoustic time averaged p'^2 from the acoustic models.

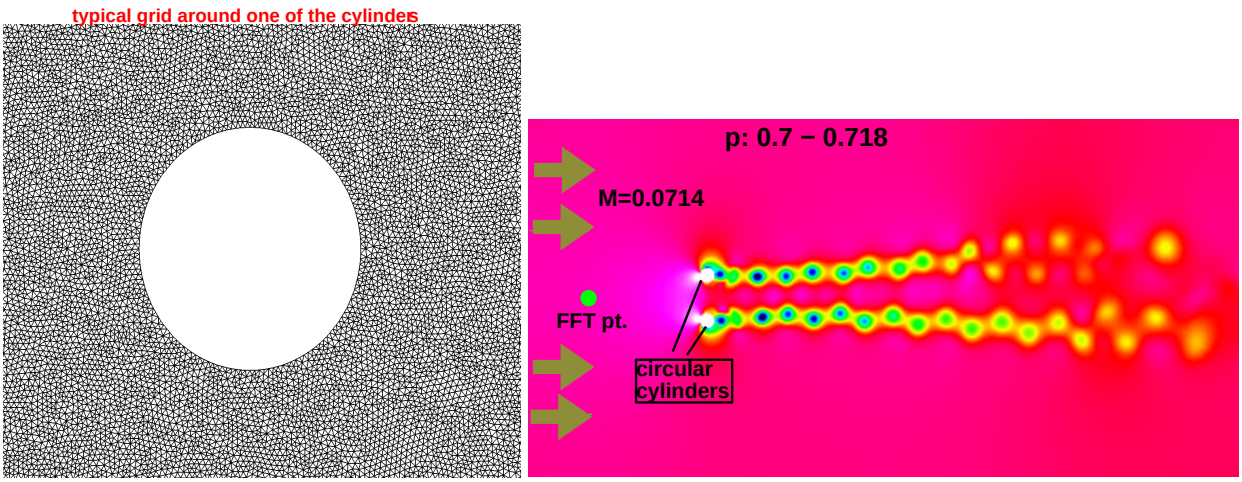

Figure 4. Left plot: Unstructured triangular grid around one of the cylinders; Right plot: Instantaneous isobars at time step 1,100,000.

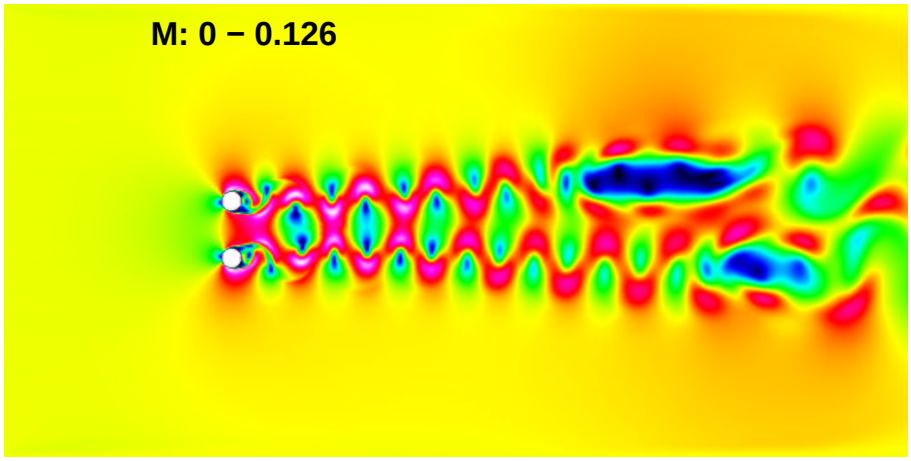

Figure 5. Instantaneous Mach No. at time step 1,100,000.

4.2 *Tone noise frequency and SPL*

Figure 7 depicts the result of the FFT, i.e., the sound pressure level (SPL) vs. frequency at a selected location $(0, 3.5D)$ for the second grid with a small domain. Again the SPL is relative to the level of 20 μPa. At a Reynolds number of 15800, the highest averaged peak of SPL in the plots corresponds to a computed Strouhal number, St, of 0.21 (with a 3dB 'bandwidth' or binwidth of 220 Hz), which is quite close to the experimental value $St = 0.205$. Figure 8 shows a plot of SPL vs. frequency for the larger domain (the first grid) but with unevenly distributed cells. The highest peak of SPL in the plot corresponds to a computed Strouhal number of 0.237 (with a 3dB 'bandwidth' or binwidth of 47 Hz), which is still reasonable, but less accurate than the the case with the second grid. Table 2 summarizes the comparison of experimental and numerical Strouhal number results. This shows that for an aeroacoustics computation, one should be cautious in choosing an unstructured grid.

5 Low-speed tone noise of a cavity with overhang (CAA Workshop III)

Cavity tone noises arise from an aeroacoustic feedback loop between the two edges of the cavity opening. At low subsonic Mach numbers (typically around or below Mach number of 0.1), or in the presence of a deep cavity, the noise due to flow-resonant phenomena occurs as well.

In the present section, for low speed flows with Mach number as low as 0.08, a cavity with an overhang at the

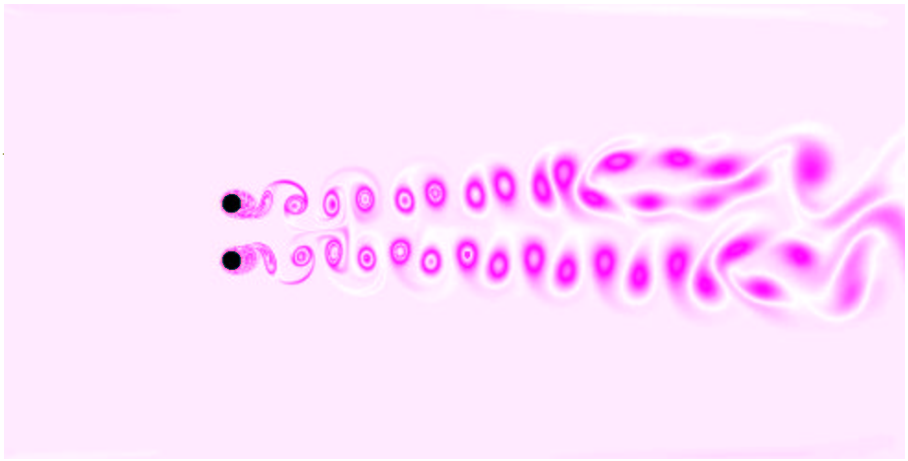

Figure 6. Vortex streets at time step 1,100,000.

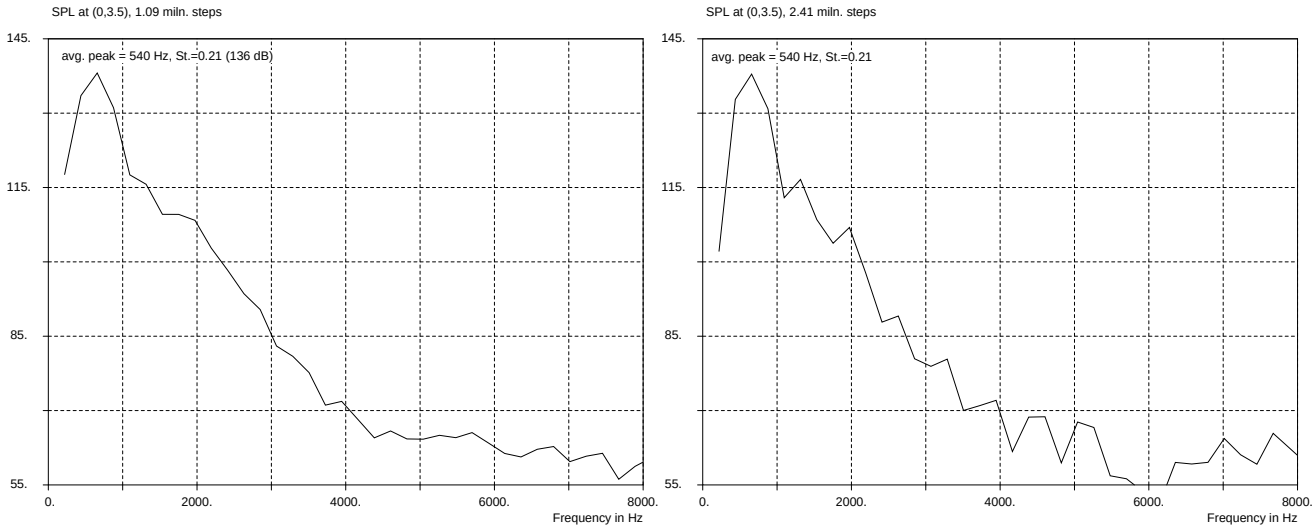

Figure 7. SPL vs. frequency at (0,3.5) for the small grid; Left plot: at time step 1,100,000; Right plot: at time step 2,400,000

Table 2. **Tone noise frequency (Strouhal No. St) vs. Re**

Re	experimental	computational (1st grid)	computational (2nd grid)
1130		St.=0.237	
15800	St. = 0.205		St. = 0.21

opening (Fig. 9) is investigated. This is a prototype of the automobile door gap noise problem [14].

Figure 9 illustrates the geometric configuration and the actual dimensions of the cavity in the noise problem. Due to the presence of the overhang tongue, the two oscillation modes, namely, the fluid dynamic oscillation related to aeroacoustic feedback, and the Helmholtz fluid resonance in the cavity may emerge at the same time and compete with each other.

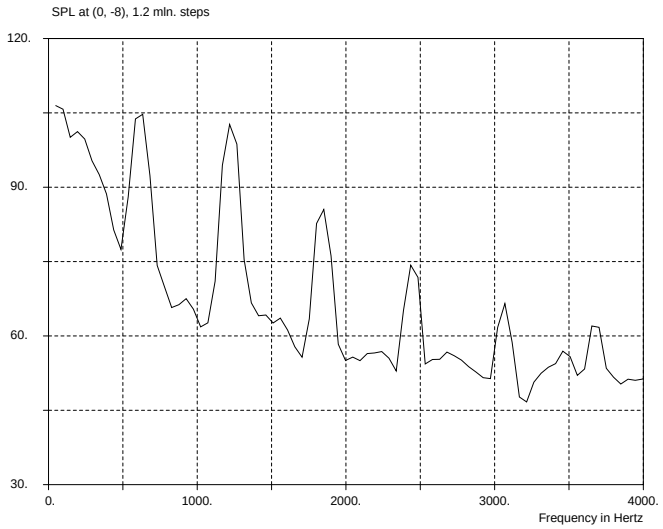

Figure 8. SPL vs. frequency at (0, -8) for the large domain.

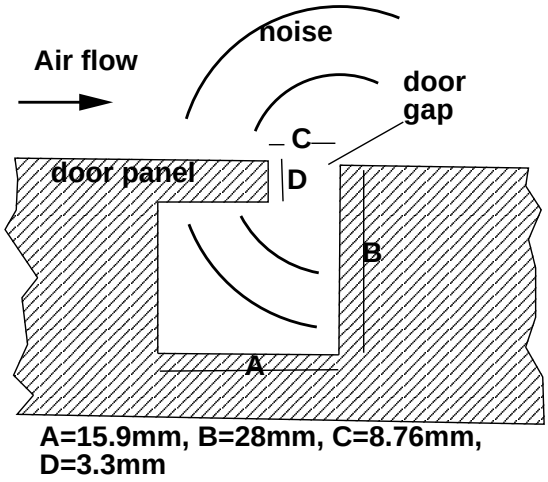

Figure 9. Auto-door gap noise problem and the cavity dimensions.

Here, C is the length of the cavity opening. The dimension 2C is chosen as the length scale. The speed of sound ($343\ m/s$) and density of the ambient flow are the scales for velocity and density, respectively. In the current computation, there are about 85300 triangulated cells in the computational domain. The domain ranges $-1 \leqslant x \leqslant 2.1$ and $0 \leqslant y \leqslant 3.2$. The triangles are actually obtained by dividing a rectangular structured mesh cell into four pieces. The rectangular cell keeps a uniform size of $\Delta x = 0.00625$ and $\Delta y = 0.00625$ around the area of the opening and the interior of the cavity, but stretches near the outer boundaries. A nondimensional time step size of 0.0025 and a weighted average (van Albada limiter) index $\alpha = 0$ is employed in the CE/SE scheme.

5.1 *Initial and boundary conditions*

The flow field is initialized to the ambient conditions:

$$\rho_0 = 1.0, \quad u_0 = 0, \quad v_0 = 0, \quad p_0 = 1/\gamma,$$

All spatial derivatives are set to zero.

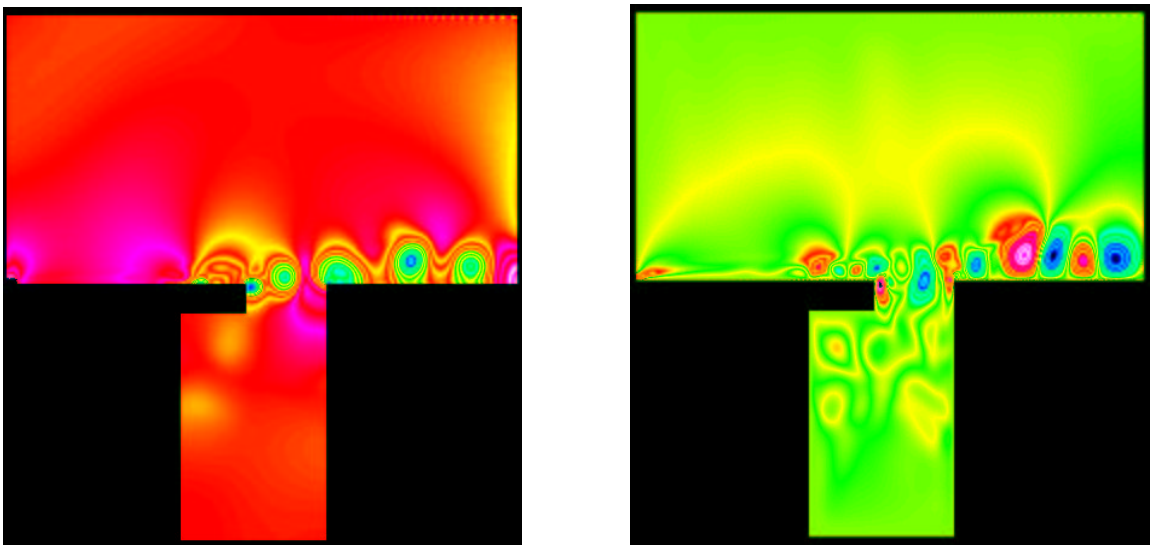

Figure 10. Left plot: Instantaneous isobars and Right plot: Instantaneous v- velocity contours at time step 740,000. Note that the color contrast is exaggerated here to highlight the flow features.

At the inflow boundary, the flow variables are specified as the uniform 'plug' flow:

$$\rho_i = 1.0, \quad u_i = M, \quad v_i = 0, \quad p_i = 1/\gamma,$$

and their spatial derivatives are set to zero. The Mach numbers range from 0.0788 to 0.147, corresponding respectively to flow speeds of 26.8 m/s and 50 m/s. When a consistency test is conducted in §5.4, a prescribed profile is imposed to the u-velocity at the inlet boundary.

The no-slip wall boundary condition is applied to all the solid walls of the cavity body. The boundary condition at the domain top is the same as that specified at the inflow, which also acts as a Type I NRBC. At the outflow boundary, The Type II NRBC is imposed.

5.2 *Numerical results*

In this section, numerical results for the low speed cavity noises are presented and compared to their respective experimental data. As designed in the experiment, all the data are obtained at a location at the center of the inner left vertical wall of the cavity.

As mentioned earlier, for the overhung cavity considered here, there are two major modes for the tone noises: the fluid dynamic tone noise due to the feedback loop around the cavity opening, and the fluid-resonant tone noises due to the Helmholtz resonance of the cavity. In addition, there could exist other tone noise modes of uncertain origins or broadband noises, making the phenomena rather complicated. For the MILES approach, Fureby [13] points out that the numerical result is relatively insensitive to the subgrid scale model used in large eddy simulation (LES) but more dependent on the grid sizes. Generally, a finer grid yields more details in the acoustic field and higher SPL. It is important to choose a grid fine enough and an appropriate weighted average index number α.

In the following, numerical results corresponding to flow speeds of 50 m/s and 26.8 m/s are presented and compared to the respective experimental data [14]. For the case with flow speed of 50 m/s, several consitency tests for the numerical work are also conducted. All the SPLs are presented in dB based on their magnitudes against the standard $20\mu Pa$.

5.3 *Noise at flow speed of 50 m/s*

Figure 10 illustrates the isobars (left plot) and v-velocity (right plot) contours at time step 740,000 with time step size of 0.0025. The unsteadiness and the large scale turbulence or instability waves are clearly displayed. It is

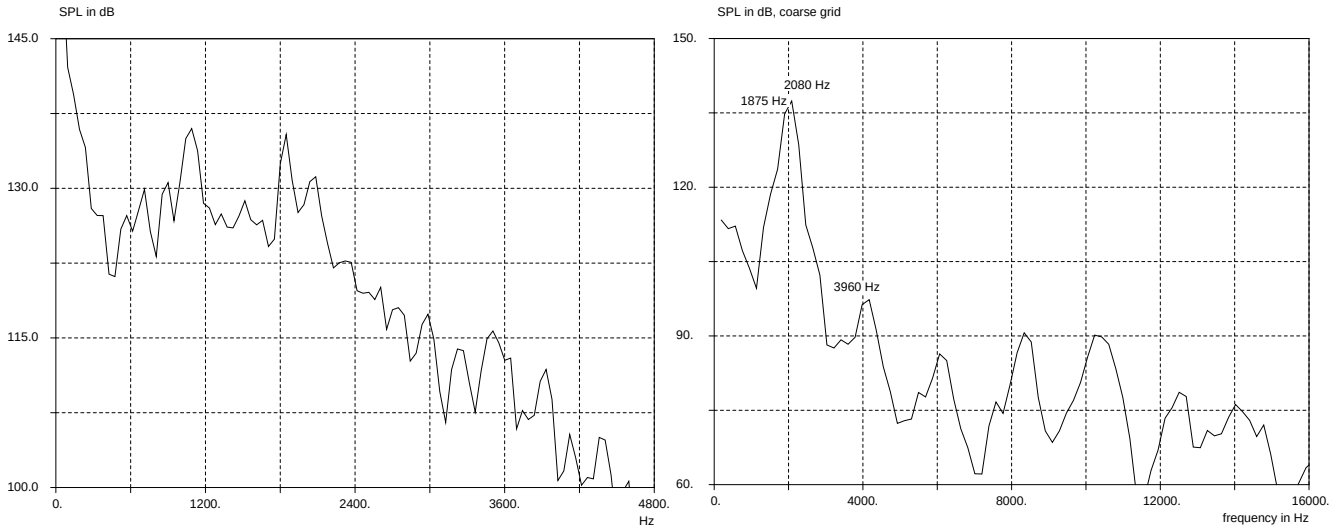

Figure 11. Left plot: Sound pressure level (SPL) vs. frequency at a low speed of 50 m/s; Right plot: SPL vs. frequency at flow speed of 50 m/s with a coarse grid.

Table 3. **Comparison of experimental and computed tone noises at 50 m/s**

Exp. Freq. Hz	Exp. SPL dB	Comput. Freq. Hz	Comput. SPL dB	Compt. Freq. Hz lrg. domain	Comput. SPL dB lrg. domain	Noise origin ? - unknown
930	103	1075	135	1062	131	?
1340	107	1326	127	1398	130	?
1824	134	1837	135	1860	129.6	feedback
2016	113	2062	130	2094	119	resonance
2848	106	2962	116	2808	111	?
3552	111	3513	115	3396	106	?

interesting to observe that the onset of the instability waves (vortices) does not occur right at the lip of the overhung tongue of the cavity, as expected for feedback oscillation, but occurs somewhat upstream. Evidently, the onset is triggered by the oscillation of cavity resonance. At the upper cavity surface around the overhung tongue, the turbulent boundary layer is disrupted and dominated by the large scale turbulence (vortices).

With a laminar uniform 'plug' flow at the inflow boundary, due to the no-slip wall boundary condition, a pulsating boundary layer is naturally formed, developed, and becomes turbulent near the overhung tongue of the cavity. No specific boundary layer thickness is given at the inlet. Table 3 provides a comparison of the experimental and computed data.

From Table 3, it is observed that for the fluid-dynamic feedback tone, the numerical results agree very well with the experimental data, 1837 Hz. vs. 1824 Hz and 135 dB vs. 134 dB. in SPL, with a binwidth (or bandwidth) of 47 Hz. The error in frequency or SPL is less than 1%, although Henderson stated that experimentally, when multiple tones occur in the spectrum, the preferred or dominant mode often changes randomly. This can result in a change of 3 dB or more in the peak sound pressure level [14]. For the Helmholtz cavity resonance, the frequencies are 2062 Hz vs. 2012 Hz with 2% error, while the error in SPL is larger. In addition, multiple tone peaks with lower SPL described

Table 4. **Comparison of experimental and computed tone noises at 50 m/s, with coarse grid**

Exp. Freq. Hz	Exp. SPL dB	Comput. Freq. Hz	Comput. SPL dB	Compt. Freq. Hz coarse grid	Comput. SPL dB coarse grid	Noise origin ? - unknown
930	103	1075	135	–	–	?
1340	107	1326	127	–	–	?
1824	134	1837	135	1875	134.8	feedback
2016	113	2062	130	2080	137	resonance
2848	106	2962	116	–	–	?
3552	111	3513	115	3960	98	?

by Henderson [14] as tones of unknown origins are also captured and fairly simulated.

Some of these tone peaks of unknown origins in Fig. 11 (left plot) and Table 3 at the low frequency end seem to be subharmonics, e.g. 1075 Hz vs. 2062 Hz. Subharmonics are often generated through vortex pairing; the excessively strong subharmonic spikes could be due to the two-dimensional simulation of a three-dimensional flow. Such spikes are absent when a coarse grid is used (Fig. 11, right plot).

5.4 *Consistency tests*

The same cavity noise problem is also tested with different grid size and computational domain to ensure that consistent and reasonable numerical results are obtained. As mentioned above, we are trying to simulate the large scale turbulence. As the grid is refined, more details of the turbulence emerge, as is experienced with many LES computations. In contrast to a deterministic flow computation problem, grid independence may *not* be tested in a rigorous way for the present noise problem due to the presence of two competing dominant modes. However, to a certain extent in a statistical way, some general agreements on frequencies may still be available for different grids. Several other consistency tests such as running with a larger computational domain and longer time, as well as imposing a specified boundary layer thickness are also conducted in the following subsections. The case presented in §5.3 will be referred to as the 'standard case' when making comparisons.

5.4.1 ***Test with a coarse grid*** This cavity noise problem at flow speed 50 m/s was calculated with a coarser grid for grid independence test. Similarly, a nonuniform rectangular grid is used before it is triangulated. Although in the refined grid area Δx =0.00625 is about the same, Δy = 0.0114 is almost twice as large in the cavity opening area compared to the grid used in the standard case. Still, good agreement with experimental data and the standard case simulation is obtained. As shown in Fig. 11 (right plot), the two shoulder points of the highest spike correspond to 1875 Hz, 134.8 dB and 2080 Hz, 137 dB. Since the binwidth (or bandwidth) is about 190 Hz in this case, it is not clear that they represent the fluid dynamic feedback oscillation or the fluid resonance mode, or both and form a broad peak. However, in terms of frequency and SPL (sound pressure level), they are in good agreement with the experimental data of 1824 Hz and 134 dB (fluid dynamic feedback) and the computed data of 1837 Hz and 135 dB with the standard case (Table 4). The grid independence is thus somehow justified.

From Fig. 11 (right plot) and Table 4, it is observed that with a coarser grid, the dominant mode frequencies match the experimental ones quite well but the SPLs are lower. The tone peaks of unknown origins (broadband noises) are muffled, but persistent higher harmonics are generated.

5.4.2 ***Test on a larger computational domain with longer run time*** In the CAA Workshop III Proceedings, several authors pointed out that the locations of the boundaries or the sizes of the computational domain have considerable effects on the noise frequencies and SPLs. In order to find out if the same phenomenon occurs with

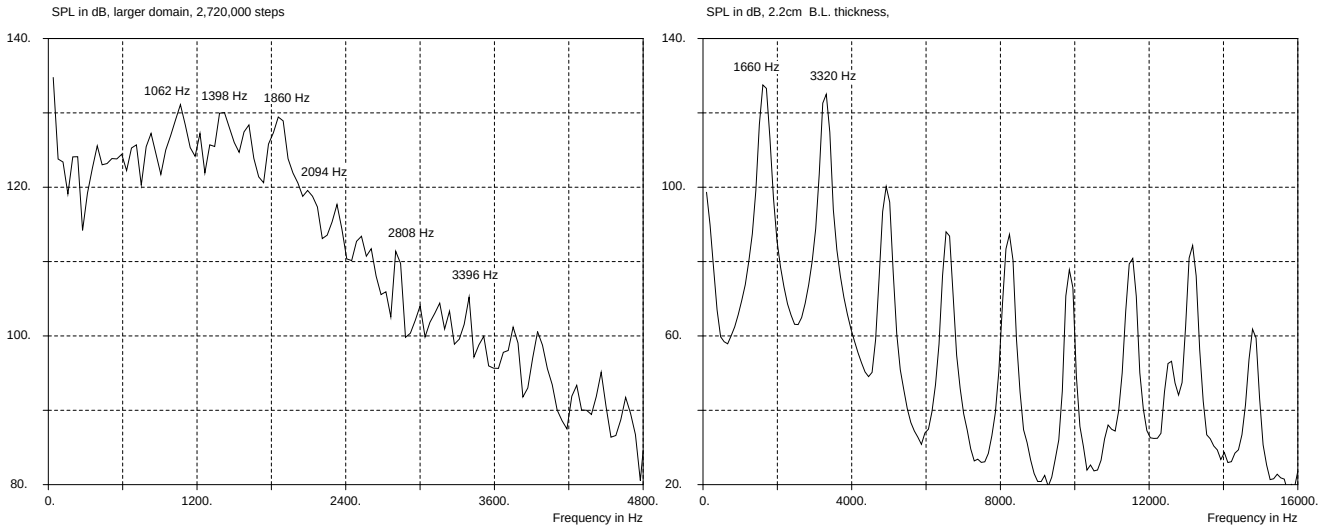

Figure 12. Left plot: SPL vs. frequency at 50 m/s with larger domain and 2,720,000 marching steps; Right plot: SPL vs. frequency at 50 m/s, with 2.2cm thick boundary layer imposed.

the present scheme, the problem is also run with a larger domain ($-2.8 \leqslant x \leqslant 4$, $0 \leqslant y \leqslant 4$), which is about 3-times larger than the grid in the standard case. The grid size in this problem is about the same as in the standard case in the critical area, i.e. the cavity interior and around the opening, but stretches faster towards the inlet, outflow and top boundaries. With a time step size of 0.003, about 2.72 million steps are run in attempt to find out the long term behavior of the simulation. The numerical results are presented in Fig. 12 (left plot). Comparisons to the experimental data and the standard case are provided in Table 3. Generally speaking, for the dominant oscillation modes, the aeroacoustic feedback and flow resonance, the error is about 2% which is quite acceptable, despite their lower SPLs as expected due to the coarser grid size. The overall performance is quite similar to the standard case in that the subharmonic-like high SPL tones appear at the low frequency portion of the spectrum, possibly due to the two-dimensional simulation for a three-dimensional flow.

It is now demonstrated that at least for the present simulation, the size of the computational domain (i.e., locations of the boundaries) and the long run time have little influence on the major numerical results, i.e., frequencies and SPLs.

5.4.3 ***Tests with artificially imposed boundary layer thickness*** In all the above numerical simulations, a simple uniform plug flow is imposed at the inlet boundary. The unsteady boundary layer develops due to the no-slip wall condition. On the other hand, it was suggested in the CAA Workshop III problem sheet that a prescribed boundary layer thickness may be used. Here, the idea is tested with the CE/SE scheme.

In this subsection, prescribed u-velocity profiles are imposed at the inlet boundary to mimic the turbulent boundary layers. Given a boundary thickness, δ, the formal u-velocity profile at the inlet boundary is specified as:

$$u = U_0(y/\delta)^{1/7}.$$

In the following two test cases, the same computational domain and grid used in the standard case are employed. In the first case, a thick turbulent boundary layer of 2.2 cm is imposed at the inlet. After 1.4 million time steps are completed, the spectrum at the assigned point on the cavity vertical wall is depicted in Fig. 12 (right plot). The prominent peaks correspond to 1660 Hz, 127 dB and 3320 Hz, 125 dB. The second peak appears to be the first harmonic of the first peak. Note that the spectrum exhibits ample high frequency harmonics of a single tone, which implies numerically that there exists a highly nonlinear wave. The pattern is quite different from that seen in the experiment [14]. In the second case, the imposed boundary layer thickness at the inlet is reduced to 1.2 cm. Figure 13 (left plot) illustrates the spectrum after 1.4 million time steps. A slightly larger time step size (0.003) is used. Here, the prominent peaks correspond to 1824 Hz, 121 dB and 3642 Hz, 124 dB. It is also noted that in Fig. 13 (left plot), to the right of the peak

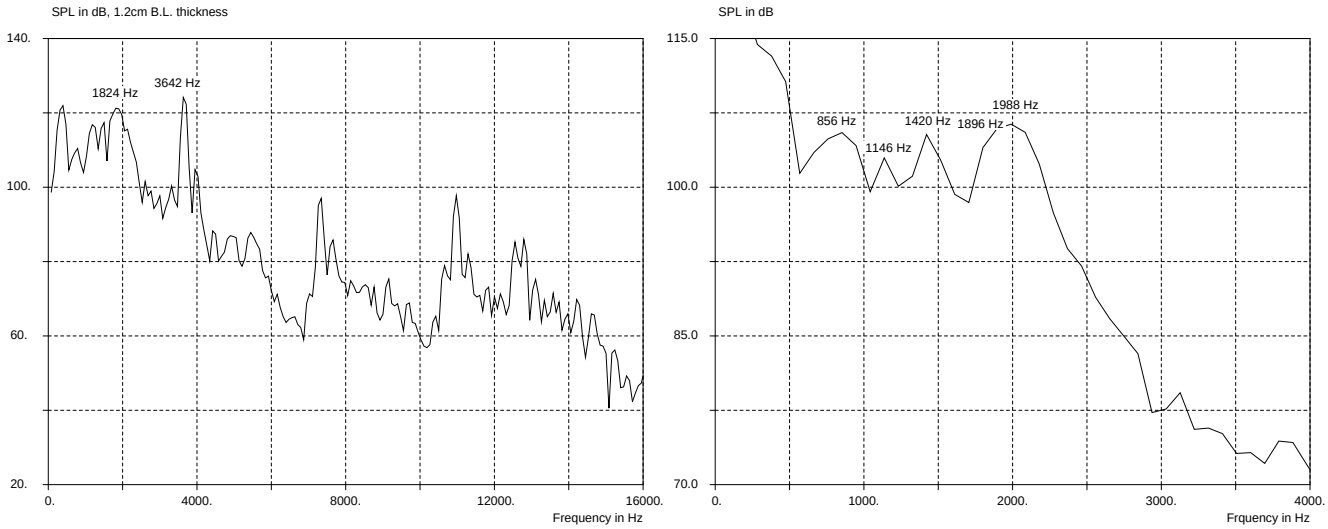

Figure 13. Left plot: SPL vs. frequency at 50 m/s, with 1.2 cm thick artificial boundary layer at inlet; Right plot: SPL vs. frequency at a low speed of 26.8 m/s.

Table 5. **Comparison of experimental and computed tone noises at 26.8 m/s**

Exp. Freq. Hz	Exp. SPL dB	Comput. Freq. Hz	Comput. SPL dB	Noise origin ? - unknown
928	97	856	105	?
1168	99	1146	103	feedback
1380	95	1420	105	?
1890	103	1896	105	?
1984	101	1988	106	resonance

at 1824 Hz, there appears a smaller peak at about 2020 Hz, which may correspond to the flow resonance frequency of 2016 Hz. In terms of frequency, the results are exceedingly good, almost agreeing exactly with the experimental data for 'thin' boundary layer [14]. There is no surprise since the boundary layer thickness of $1.2cm$ matches the experiment exactly. However, in terms of SPL, the numerical values are still low probably due to insufficient grid resolution. In addition, high SPL unwanted peaks appear at the low frequency end of the spectrum possibly due to the two-dimensional simulation.

The numerical experiments show that the prescribed boundary layer thickness has considerable effect on the spectrum and SPL. Without any knowledge or hint about the boundary layer, an arbitrarily prescribed boundary layer thickness may not work well; and it is probably best to let the flow develop its own.

5.5 *Noise at flow speed of 26.8 m/s*

Numerical experiments are also conducted for a lower flow speed of 26.8 m/s given the same cavity geometry. Table 5 lists a comparison of the experimental and computed data. As in the standard case, uniform plug flow is imposed at the inlet boundary.

From Table 5, it is observed that for the fluid-dynamic feedback tone, the numerical results agree very well with

the experimental data, 1146 Hz. vs. 1168 Hz and 103 dB vs. 99 dB in SPL, with a binwidth (or bandwidth) of 95 Hz. The error in frequency or SPL is about $3-4\%$. For the cavity resonance, the frequencies are 1988 Hz vs. 1984 Hz with 0.2% error, and the SPLs are respectively 106 dB and 101 dB. There are also other noise tones of unknown origin. The errors in frequencies and SPLs with these computed tones are larger. Similar to the standard case, their SPL are relatively high, possibly due to the two-dimensional simulation of a three-dimensional flow. From Fig. 13 (right plot), there is probably another tone of unknown origin - the one at 1896 Hz. Its frequency is so close to the resonance frequency 1988 Hz and the binwidth is 95 Hz, that it becomes difficult to distinguish the two frequencies. The two frequency spikes coalesce into a single broad peak. According to the experimental observation of Henderson [14], well defined discrete frequencies do not appear consistently until the flow velocity reaches 35 m/s. Based on this argument, the numerical results for the lower flow speed are indeed in very good agreement with the experiments.

6 Concluding Remarks

In this paper, a MILES type numerical approach - the CE/SE scheme, is adopted to simulate the tone noises arising from large scale turbulence generated in viscous flows. No explicit turbulence or subgrid models or acoustic models are used.

For the three benchmark CAA Workshop problems considered in this paper, generally good results are obtained and compare favorably to the experimental data. However, a two-dimensional simulation of a three-dimensional flow may generate some excessively strong subharmonics towards the lower end of the spectrum. Particularly for the cavity noise problem, as there are two dominant oscillation modes - aeroacoustic feedback and flow resonance competing with each other, accompanied by some tones of unknown origins, or broadband noise, it is important to select carefully the grid size and other parameters in the computations.

In the MILES type approach, we attempt to simulate only the large scale turbulence, which is believed to be the tone noise generating source. The smaller scale turbulence (higher frequencies and wave numbers) are practically ignored without an explicit subgrid scale model, since we are interested primarily in the aeroacoustic data. The CE/SE method is a scheme for solving conservation laws. When the divergence theorem (2) is applied to find the cell average, it also plays a role as a filter (such as the one used in LES approach). High frequency and high wave number disturbances are filtered out and aliasing errors are unlikely to occur. As pointed out by Fureby [13], choosing the parameters or limiters in the MILES approach, is somewhat equivalent to choosing a subgrid scale model in the conventional LES approach. The choice is not straightforward in the presence of complicated flows.

Acknowledgements

This work received support from the Supersonic Propulsion Technology Project Office of NASA Glenn Research Center.

References

[1] Chang, S.-C., Wang, X.-Y. and Chow, C.-Y., "The Space-Time Conservation Element and Solution Element Method—A New High Resolution and Genuinely Multidimensional Paradigm for Solving Conservation Laws," J. Comp. Phys. vol. 159, pp. 89-136 (1999).

[2] Wang, X.-Y. and Chang S.-C., " A 2-D Non-splitting Unstructured Triangular Mesh Euler Solver Based on the Space-Time Conservation Element and Solution Element Method" C.F.D. J. vol. 8, pp309-325 (1999).

[3] Loh, C. Y., "On a Nonreflecting Boundary Condition for Hyperbolic Conservation Laws" AIAA Paper 2003-3975 (2003).

[4] Loh, C. Y., "Near Field Trailing Edge Tone Noise Computation" AIAA Paper 2003-0365 (2003).

[5] Loh, C. Y., Hultgren, L. S. and Chang S.-C., "Computing Waves in Compressible Flow Using the Space-Time Conservation Element Solution Element Method," AIAA J., Vol. 39, pp. 794-801 (2001).

[6] Loh, C. Y., Hultgren, L. S., and Jorgenson, P. C. E., 'Near Field Screech Noise Computation for an Underexpanded Supersonic Jet by the CE/SE Method', AIAA Paper 2001-2252, (2001).

[7] Loh, C. Y. and Zaman, K.B.M.Q., " Numerical Investigation of Transonic Resonance with a Convergent-Divergent Nozzle", AIAA J., Vol. 40, No. 12, pp. 2393-2401 (2002).

[8] Loh, C. Y., Himansu, A., and Hultgren, L.S., “A 3-D Navier-Stokes Solver with Unstructured Hexahedral grid for Computations of Near Field jet Screech Noise” AIAA Paper 2003-3207 (2003).
[9] C.K.W.Tam, J.C.Hardin, Eds., “Second Computational Aeroacoustics (CAA) Workshop on Benchmark problems”, NASA CP-3352, June,1997.
[10] H.Schlichting, ‘Boundary-Layer Theory’, McGraw Hill, 1979.
[11] A.A.Townsend, ‘The Structure of turbulent Shear Flow’, 2nd edition, Cambridge University Press, 1976.
[12] J.P.Boris, F.F.Grinstein,E.S.Oran, and R.J.Kolbe, “New Insights into Large Eddy Simulation”, Fluid Dynamics Research, vol.10, No.4-6, pp.199-227, 1992.
[13] C.Fureby and F.F.Grinstein, “Monotonically Integrated Large Eddy Simulation of Shear Flow”, AIAA J. , vol.37, No.5, pp.544-556, 1999.
[14] B. Henderson, “Category 6, Automobile Noise Involving Feedback-Sound generation by Low Speed Cavity Flows”, in “Third Computational Aeroacoustics (CAA) Workshop on Benchmark problems”, NASA CP-2000-209790, August, 2000.
[15] Loh, C. Y., Chang, Sin-C., Wang, X.-Y. and Jorgenson, P. C. E., “Gap Noise Computation by the CE/SE Method” ASME paper, FEDSM-2001-18136.